33RD CONGRESS
OF THE INTERNATIONAL COUNCIL
OF THE AERONAUTICAL SCIENCES
STOCKHOLM, SWEDEN, 4-9 SEPTEMBER, 2022

ICAS 2022 SWEDEN

A STUDY OF HIGH-LIFT DEVICES FOR LOW REYNOLDS NUMBER APPLICATIONS

Abstract

This paper presented a study on low Reynolds number high-lift trailing edge devices to facilitate take-off and landing performance improvement of small unmanned aerial vehicles (sUAV). Little researches have been conducted at Reynolds number range of 1×10^5, where the boundary layer's load carrying capability is reduced. Furthermore, simplicity and robustness dictated the use of such devices on sUAV. This study employed existing semi-empirical method to prototype a single- and double-slotted flap for a DAE31 low Reynolds number airfoil. The detailed designs were tested in low-speed windtunnel and analysed through URANS simulations. The scope of the paper was to survey the applicability of available design tools and to provide a detailed analyses of aerodynamic phenomena on such type of high-lift devices.

Keywords: High-lift devices, low Reynolds number, unmanned aerial vehicle.

1. Introduction

High-lift devices have been extensively studied and used at the scale of commercial and light aircraft, however there is insufficient research in the behaviour of these devices at low Reynolds number in the order of 1×10^5. This regime of flow is particularly of interest for small Unmanned Aircraft Systems (sUAS) applications under 25kg, notably allowing for short take-off and landing to better adapt for various constrained operation fields. There are numerous types of high-lift devices as illustrated in Fig. 1. They are chosen based on the aircraft scale as well as the required performance. This study is driven by the need for reduced landing distance, consequently flap deflections were able to achieve $30°$ to $40°$.

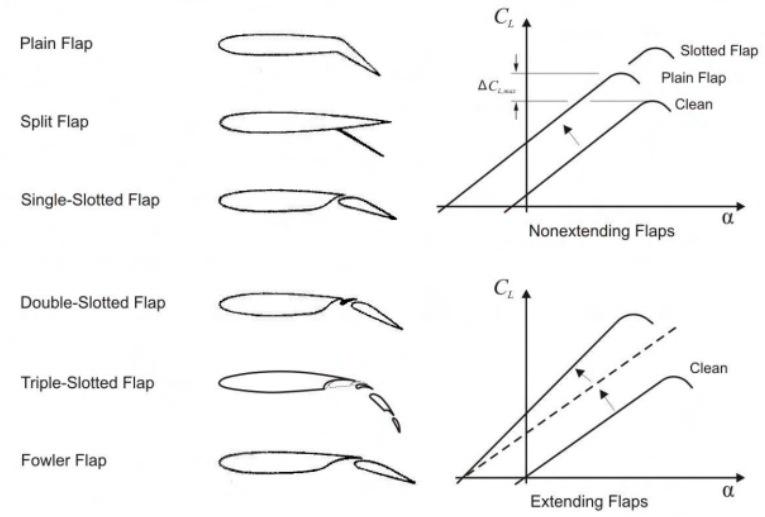

Figure 1 – Various types of high-lift devices, illustrations from DATCOM [1]

For the application of sUAS, simple mechanisms are preferred for reliability and ease of manufacturing. In the scope of the current study, plain flaps, single- and double-slotted hinged flaps are

investigated. Their performance is estimated using empirical method, quasi-2D wind tunnel test as well as 2D and 3D computational fluid dynamics (CFD) simulations. Various deflection angles and gap sizes were studied.

When fully deployed, high lift coefficients C_L is expected, as well as a relatively high C_D. This implies large perturbations in pressure distributions, which could introduce error in small windtunnels typically employed for sUAS research. A full CFD simulation of the test section has been performed to identify and quantify these errors to facilitate future studies.

The current study aims to provide a clear view of available analytical and experimental approach in low Reynolds number high lift device analysis. Section III presents a survey of previous studies of high lift devices, and demonstrates current limited scope in low Reynolds number applications. Section IV provides an analytical analysis using available design approaches for a proposed high lift configuration, and the experimental as well as numerical studies on the designs are presented in Section V and VI. The study will conclude the applicability and potential corrections of available method applied to low Reynolds number conditions.

2. Past Studies

The theoretical explanation of high lift devices, especially for multi-element airfoil, was systematically developped in Ref. [2]. Smith has explained the pressure recovery limit of single airfoil and its implication in guiding high lift airfoil design. He further pointed out that the aerodynamic interaction between multiple airfoil elements work to distribute suction peak between elements to relief pressure recovery margin over each single airfoil, which results in overall higher lift coefficients. Smith's work serves as a theoretical guide for further development of high-lift devices at high Reynolds number, however the limited database means his work could not be used in practical design applications.

Various NACA and further NASA studies [3, 4, 5, 6] have accumulated valuable experimental data for various high-lift device configurations. These studies confirmed the effectiveness of multi-element airfoil in improving maximum lift coefficient, which could be increased well over 2.5 for slotted flaps. These studies also pointed out that the boundary layer condition at the slot between elements is critical for lift enhancement [7]. Characteristics of boundary layer at operating condition is sensitive to viscous effects, which can be characterised from Reynolds number Re. However only limited data could be accessed for low Reynolds number $Re \leq 5 \times 10^5$ for typical sUAS operation.

For small-scale applications such as sUAV or light aircraft, simplicity in manufacturing and handling usually prevented the adoption of high lift devices other than plain or split flap [7]. Therefore, the pursuit for high lift resorts either to powered circulation control system [8] or to use specifically designed airfoil [9], which don't include complicated exterior articulation mechanism but is more difficult to compromise between cruise and high-lift performances. As manufacture technology advances with the growing interest in sUAV, recent studies have looked at fixed leading edge devices in low Reynolds number regime [10], as well as Fowler flaps [11] based on 4-link mechanism. These studies have shown that significant lift enhancement still could be achieved with existing high-lift system principles, but the expected performance departs from observations in higher Reynolds number and depends particularly on the implementation of actuation mechanism.

Calculation methods for multi-element airfoil design are also limited. Semi-empirical method could be found in ESDU reports [12, 13], the method considers various geometry parameters to correct for the lift enhancement effect of trailing and leading edge devices. The applicability of the method however is only verified for $Re \leq 1 \times 10^6$. Another semi-empirical approach is proposed in Ref. [14], which is also aimed at high Reynolds number applications and is integrated in stability analysis platform DATCOM. Higher fidelity methods include MSES [15] which was coupled with a integral boundary layer formulation to for relatively low Reynolds number treatment.

3. Empirical Methods

The initial geometry of trailing edge device is analysed through empirical methods [13, 14, 16] based on previous experimental data. These were all obtained at high Reynolds number regime between $1 \sim 9 \times 10^6$, and therefore the results could only be referenced as a maximal limit for intended design. Nevertheless, these analytical approaches are fast to perform, and thus allow for rapid parametric studies at early design stage of high lift devices.

Figure 2 – DAE31 airfoil

The current research focuses on the DAE31 airfoil depicted in Fig. 2 as the baseline profile. It was developed and used for Daedalus human powered aircraft, in order to achieve high cruise efficiency[17]. The aerodynamic polar calculated from XFOIL is shown in Fig. 3b, which indicates maximal 2D lift to drag ratio of 78 at Reynolds number 3.0×10^5. For maximal lift coefficient, the airfoil is able to achieve $C_{L_{m0}} = 1.64$ at 15° angle of attack. Typical landing constraint of fixed wing drone would desire $C_{L_{m0}} \geq 1.8$ depends on specific applications, and thus it is necessary to enhance the airfoil's lifting performance with a high lift device.

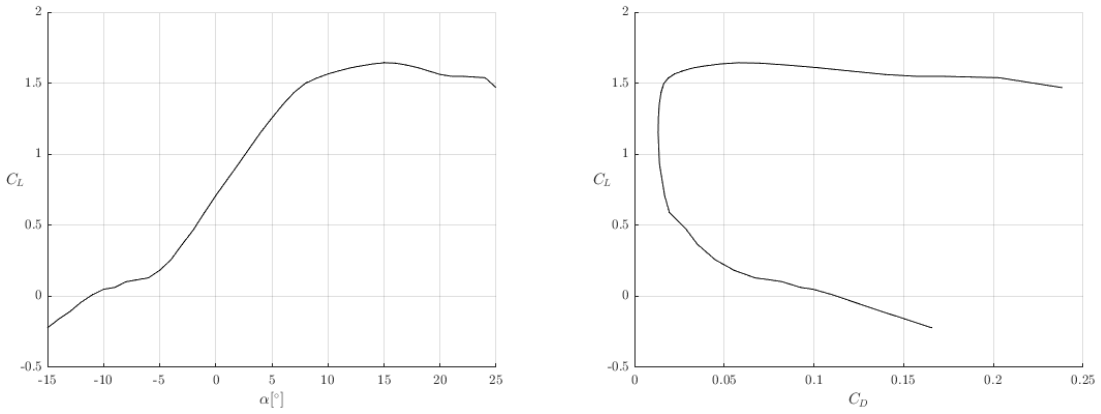

(a) Lift coefficient curve

(b) Aerodynamic polar

Figure 3 – DAE31 airfoil characteristics at $Re_c = 3.0 \times 10^5$ from XFOIL calculations

Two well established methods have been performed on the same flap geometries, the first approach is presented in ESDU documentation [16] and a second approach can be found in DATCOM [14]. This section presents a brief introduction of both methods, followed by the preliminary lift augmentation estimation on a DAE31 airfoil. The general assumptions for trailing-edge device are listed in Table. 1.

$\bar{c}_f$	0.3
δ_f	30°
Re_c	3×10^5

Table 1 – Flap design parameters

3.1 ESDU method

The necessary equations and dataset to estimate incremental lift on plain, single- and double-slotted flap were documented in reports 5c. 94028, 94030 and 94031. These constitute an semi-empirical approach for assessing maximal lift coefficient with trailing-edge devices.

3.1.1 Plain Flap

The increment in maximum lift coefficient for plain flap is given in Eq. 4.8 in item 5c. 94028 as following

$$\Delta C_{L_{mf}} = K_G K_t T \Delta C_{L_{0t}} \tag{1}$$

where K_G is empirical factor for airfoil leading edge radius, K_t is empirical factor for flap deflection and T is thin airfoil estimation of the ratio between increment in maximum lift coefficient and increment in zero angle of attack lift coefficient ΔC_{L0t}, which is estimated from flap deflection and flap chord length using equation extracted from the same report :

$$\Delta C_{L_{0t}} = 2J_p\delta_f\left[\pi - \cos^{-1}(2\bar{c}_t - 1) + \sqrt{1-(2\bar{c}_t-1)^2}\right] \tag{2}$$

where J_p is in function of the sum of flap angle and the angle between the airfoill datum and the tangent to the upper surface at the trailing edge.
To account for Reynolds number effect, the increment in maximal lift coefficient is multiplied by a Reynolds number factor

$$F_R = 0.153\log_{10}Re_c \tag{3}$$

which is based on reference Reynolds number $Re_c = 3.5\times10^6$.
Based on the DAE31 airfoil performance and flap design parameters given in Table. 1, the increment in maximum lift coefficient is estimated to be 0.48 at $Re_c = 2.3\times10^5$, and thus maximum lift coefficient can be estimated to be 2.12.

3.1.2 Single-Slotted Flap

The increment in maximum lift coefficient for single-slotted flap is given in Eq. 4.9 in item 5c. 94030 as following

$$\Delta C_{L_{mf}} = \left(1 - c/c'\right)(1-\sin\delta_t)C_{L_{m0}} + K_T K_{t_1} J_{t_1}\Delta C'_{L1} \tag{4}$$

where $C_{L_{m0}}$ is base airfoil maximum lift coefficient at $Re_c = 3.5\times10^6$; c' is the extended chord length; and J_{t1}, K_T, K_{t1}, $\Delta C'_{L1}$ are correction factors found in the report.
The calculated ΔC_{Lmf} should also be corrected for Reynolds number effect using the same correction factor F_R.
With the same assumption for flap deflection and flap chord length, and assuming the slotted flap extends total chord by 15% at $\delta_f = 30^\circ$, the increment in maximum lift coefficient is calculated to be 0.587 at $Re_c = 2.3\times10^5$ with $C_{L_{mf}} = 2.23$.

3.2 DATCOM method

Another semi-empirical approach is summarised in Ref. [1] for assessment of various trailing-edge devices. The increment of lift coefficient for these is calculated by

$$\Delta C_{L_{mf}} = k_1 k_2 k_3 \left(\Delta C_{L_{mf}}\right)_{base} \tag{5}$$

where $\left(\Delta C_{L_{mf}}\right)_{base}$ is the increment in maximum lift coefficient for a reference 25% flap, k_1 is a correction factor for flap chord length, k_2 and k_3 are correction factor for flap angle determined in Ref. [14] from flap configuration and its design parameters.
The coefficients and estimated performance of plain and single-slotted flap are summarised in Table. 2, combined with results obtained previously with ESDU method.

	Plain Flap		Single-Slotted Flap	
Method	DATCOM	ESDU	DATCOM	ESDU
$(\Delta C_{L_{max}})_{base}$	0.85	-	1.22	-
k_1	1.05	-	1.05	-
k_2	0.76	-	0.86	-
k_3	1.0	-	1.0	-
$\Delta C_{L_{mf}}$	0.68	0.48	1.10	0.59
$C_{L_{mf}}$	2.32	2.12	2.75	2.23

Table 2 – Lift enhancement of trailing edge devices from semi-empirical methods

The method doesn't propose Reynolds number correction and the estimations are considerably more optimistic than that from ESDU method. The large difference between the methods thus justifies detailed analysis from experimental and high resolution numerical methods.

4. Mixed-inverse Design

The empirical methods provided initial estimations with expected performances of high-lift devices, however they were unable to inform detailed geometry design. When deployed the wing section equipped with flap will be operated at $Re \approx 3 \times 10^5$, coupled with large deflection angle, viscous effects is of great concern when shaping the flap airfoil. In high-lift configuration, the airfoil will need to sustain large pressure gradient which tends to destabilise boundary layer and promotes flow separation. This is especially the case at lower Reynolds number where the boundary layer thickness is larger and more susceptible to adverse pressure gradient. Therefore, it was concluded that the preliminary design method must include viscous phenomena that is able to at least treat limited flow separation. MSES is such a tool that achieves compromise between computational efficiency and fidelity in flow physics. The flow domain around the airfoil is discretised and solved using Euler equations. This allows the existence of shear layer, however viscous terms are still not included at arbitrary space. The boundary layer is thus resolved separately from integral relations, which allow calculation of viscous drag and viscous displacement effect. The formulation uses envelope method for transition prediction and is admissible to limited flow separation including separation bubbles.

4.1 Design procedure

The design for the double-slotted flap was aided by the mixed-inverse design routine of MSES. The baseline DAE31 airfoil was separated manually into three parts : 1) main element; 2) flap vane element; and 3) flap element. An initial calculation is required to serve as the starting point of inverse design procedure. The pressure distribution on three elements are then analysed and modified in an iterative fashion :

1. Check pressure peak and recovery on flap element, if desirable, the procedure is considered terminated.

2. Otherwise, check pressure distribution on vane, if it doesn't present major flow separation, re-prescribe the leading edge pressure distribution on flap element so a more gradual pressure gradient can be achieved.

3. Otherwise, reshape vane pressure distribution to eliminate or greatly minimise separation.

The procedure involves principally modification to the vane and flap leading edge section so that cruise performance won't be significantly altered as these surfaces are embedded when the mechanism is retracted. For the same reason, the main element remained unchanged except when reshaping is required for the slot entry to clear interference.
Given the limitations of MSES formulation, the design procedure is based at chord Reynolds number $Re = 3.0 \times 10^5$ and angle of attack $\alpha = 2°$, with $\delta_f = 20°$. The design procedure always yielded significant improvement of lift coefficient over initial design, however it should be mentioned that the maximum lift coefficient could be even higher since $C_{L_{max}}$ of such high-lift configurations is always achieved with a certain amount of separated flow beyond the capability of MSES. Thus the angle of attack and/or flap deflection angle at $C_{L_{max}}$ might differ from the design point.

4.2 Location of flap element

The effect of flap element position can also be examined in MSES at design and off-design conditions. Having determined the flap geometry and deflection angle, the flap element is being placed according to two parameters : 1) overlap length $\bar{x}_c$ between flap leading edge and main element trailing edge and 2) gap size $\bar{z}_g$, which is defined as the shortest distance from main element trailing edge to the flap upper surface. Figure 4 clearly demonstrates the definition of flap position.

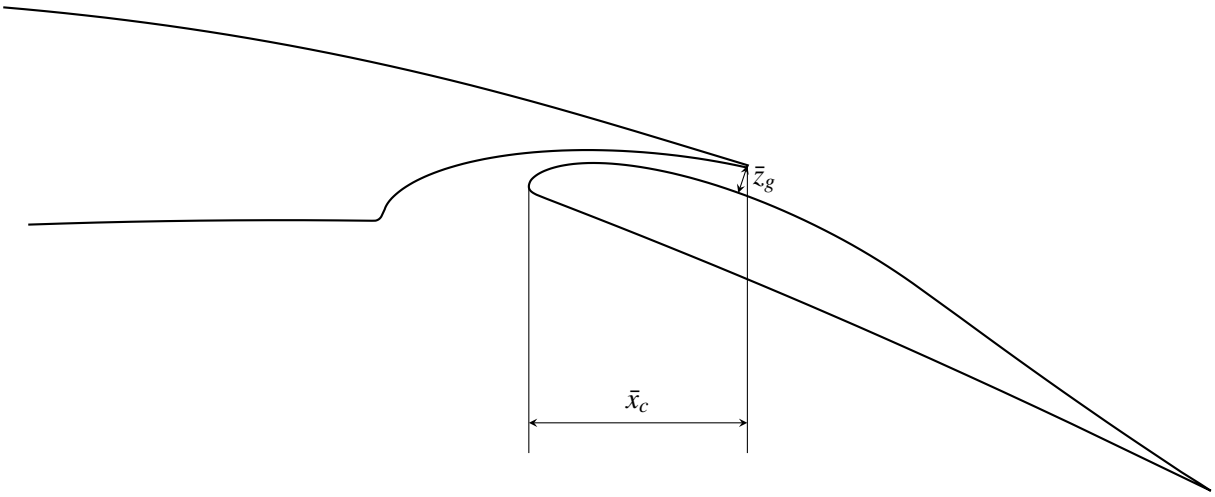

Figure 4 – Flap overlap length and gap size

In this study, the single-slotted flap performance was estimated using MSES at different $\bar{x}_c$ ranging from 0% to 10% and $\bar{z}_g$ from 1.5% to 3%. To demonstrate the effect of both $\bar{x}_c$ and $\bar{z}_g$, the calculation results are presented as iso-C_L lines in Fig. 6.
Solid line represents lift coefficients obtained under design Reynolds number of 3×10^5. A peak value over 2.3 is found to be at $\bar{x}_c = 2.5\%$ and $\bar{z}_g = 1.5\%$. C_L would decrease at a larger gap size or a different overlap length.
Lift coefficients obtained at higher Reynolds numbers $Re = 5\times10^5$ and 1×10^6 are depicted as dashed and pointed isolines. As the Reynolds number increases, the contour tends to become verticle at $\bar{x}_c > 5\%$, suggesting that the gap size has less influence in this region.
Figure. 5 plots the total boundary layer thickness δ^* of main element's lower surface and flap element's upper surface at the main element's trailing edge. The curves were all calculated with $\bar{x}_c = 2.5\%$, and show evolution of boundary layer displacement effects under three tested Reynolds numbers. At $\bar{x}_c = 2.5\%$, the gap size has the greatest effect at $Re = 3\times10^5$ where δ^* grows by 46% as gap size increases from 1.5% to 3%. At the $Re = 1\times10^6$ the growth of displacement thickness with gap size is less significant hence less effect of gap size on C_L.

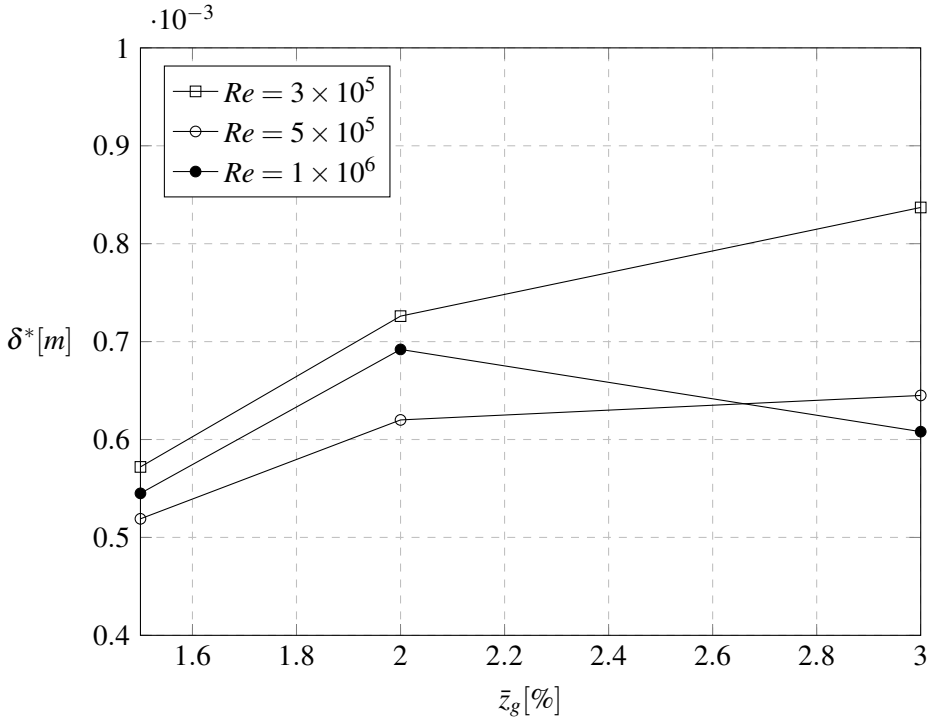

Figure 5 – Total displacement thickness at main element trailing edge with $\bar{x}_c = 2.5\%$

The effect of Reynolds number shows that the optimal position of flap element to maximize C_L could be differently influenced. At high Reynolds number, a smaller or negative overlap could be adopted while gap size has a secondary effect; at low Reynolds number, gap size and overlap length should coupled to achieve the maximal C_L for a given flap deflection angle.

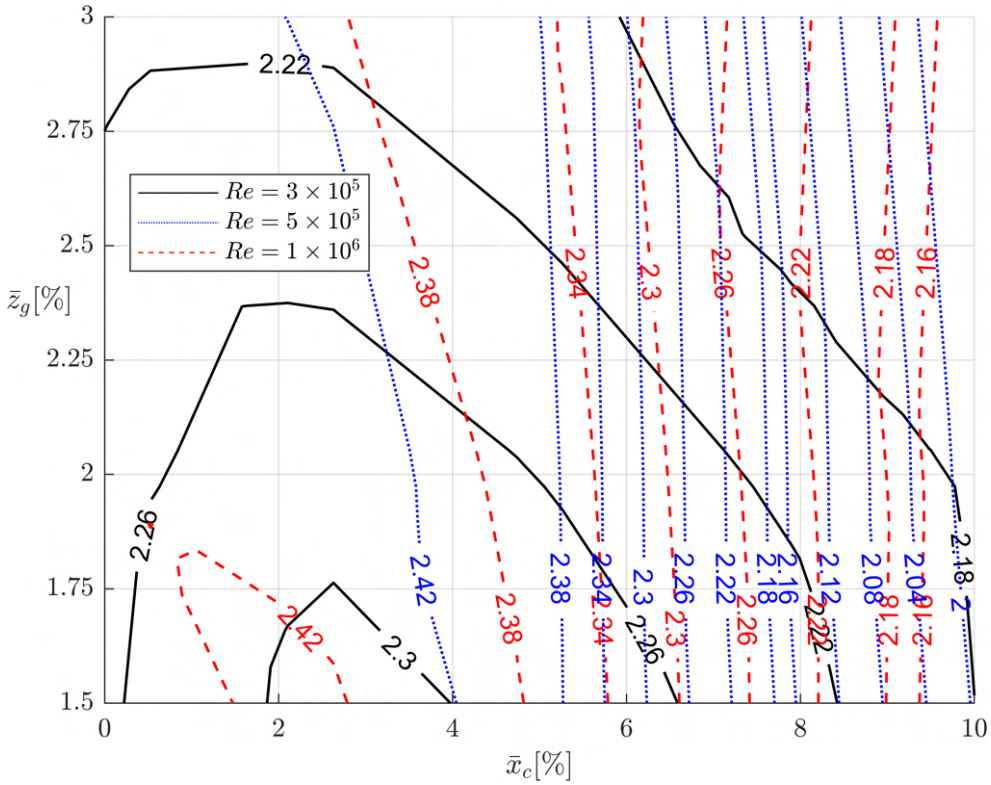

Figure 6 – Single-slotted flap lift coefficient at various $\bar{x}_c$, $\bar{z}_g$ and Re, $\alpha = 2°$, $\delta_f = 20°$

5. Flap Designs

Based on analysis in section 3and section 4.two flap geometries were designed for detailed study. The single-slotted flap makes up the last 30% chord of the airfoil. The leading edge is based on DAE31 profile and blends smoothly with the main airfoil trailing edge. The geometry is illustrated in Fig. 7. Point H is the hinge location which is offset by 15% chord below the airfoil to provide the necessary chord extension. The offset hinge mechanism is preferred than a 4-link or track mechanism thanks to its simplicity in fabrication.

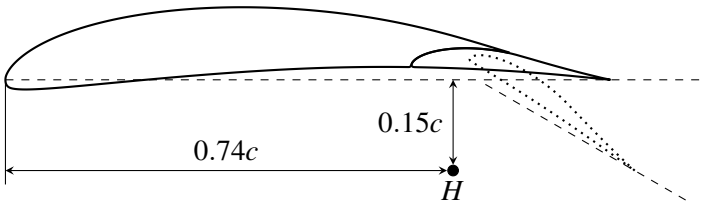

Figure 7 – DAE31 airfoil with single-slotted flap

The double-slotted flap is designed with multi-element airfoil design tool MSES which is a Euler solver coupled with integral boundary layer formulation. The design tool is capable of inverse airfoil design from specified pressure distribution and includes treatment for laminar-turbulent separation bubble and limited seperated flow. The first element starts from 60% chord length and spans 18% chord; the second element starts from 74.5% chord and is 25.5% chord in length. The two flaps elements connected in a solid fashion, meaning that they would rotate at the same angle when deployed and the gap size between them remains unchanged. The geometry is depicted in Fig. 8, noted that the gaps between airfoil elements don't close during cruise. Three hinge positions denoted H_1, H_2 and

H_3 are planned to be tested to investigate the effect of gap size between the main airfoil and the first element.

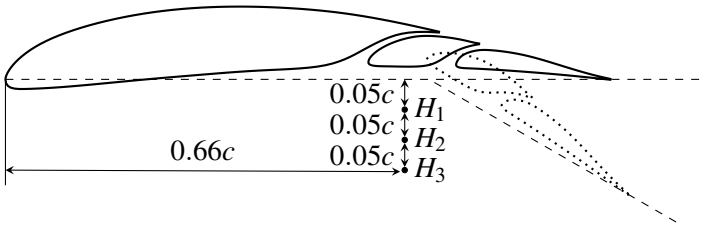

Figure 8 – DAE31 airfoil with double-slotted flap

6. Experimental Analysis

The plain flap, single- and double-slotted flap geometries have been established in the previous sections using reduced-order methods that are conventionally used for higher Reynolds number regime, discrepencies are thus expected and must be quantified in experimental conditions. This section describes the manufacture, testing and synthesis of previously proposed high lift devices.

6.1 Experimental setup

The experiments were conducted at ISAE subsonic wind tunnels in the Department of Aerodynamics, Energetics and Propulsion (DAEP). These are Prandtl type wind tunnels with a square test section of $0.45m$ sides and $0.7m$ long. A pitot tube is placed ahead of the model in the convergent section of the tunnel and allows for a measurement of wind speed. Since the tube is placed at the end of convergent section and not in the test section, a correction factor based on the test section geometry is applied to obtain the actual velocity in the test section. The measurement system is a 6-axe scale with max load of $30N$ placed outside the test section with three profiled supports protruding into the test section. Each model is 3D printed allowing for high accuracy in the airfoil shape and has three mounting points. It is mounted on to the masts with two of the masts being fixed and one mobile for adjusting the model's angle of attack. Two plexiglas end plates are mounted to both sides of the model to obtain quasi-2D flow on the wing section.

Airfoil	DAE31
Chord c	$170mm$
Span b	$300mm$
Aspect Ratio λ	1.76

Table 3 – Clean model dimensions

Three sets of models were studied in the current paper. The flapless configuration is a single DAE31 section with its dimensions given in Table. 3, whose purpose is to validate the experiment apparatus with computational method. The single- and double-slot flap designs take the same overall dimension as the flapless configuration but consist of respective trailing edge devices described in section 5. The main wing section and flap were fabricated separately through addictive manufacturing. The model doesn't include an actuation mechanism, and the flap angle was adjusted by fixing the flap hinge at different positioning holes on the end plate as demonstrated in Fig. 9a and Fig. 9b.

(a) $\delta_f = 10°$ (b) $\delta_f = 40°$

Figure 9 – Single-slotted flap model at ISAE low-speed wind tunnels

For the double-slotted flap, additional positioning holes were drilled to investigate the effect of first gap size. This is achieved by moving the hinge position perpendicular to the clean airfoil's mean chord line. Three locations were tested at $\bar{z}_h = -5\%$, -10% and -15%, where the negative sign signifies that the hinge point is located below the mean chord line. The model setups for $\bar{z}_h = -10\%$ and -15% are shown in Fig. 10a and Fig. 10b.

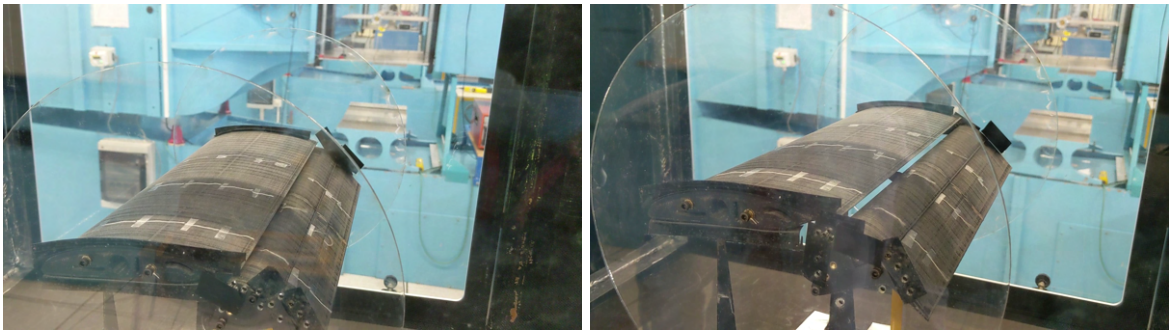

(a) $\bar{z}_h = -10\%$ (b) $\bar{z}_h = -15\%$

Figure 10 – Double-slotted flap model at $30°$ flap setting and two hinge positions

As a result of the proximity of the positioning holes, it has been decided that the single-slotted flap would be deployed at $\delta_f = 10°$, $20°$, $30°$ and $40°$ while the double-slotted flap would be deployed at $\delta_f = 15°$, $30°$ and $45°$. The comparison of these two configurations would therefore only be made for $\delta_f = 30°$ in subsection 6.6

6.2 Preliminary runs for calibration

To find the setup that best represents 2D condition, three different setups with the flapless model were tested at $15m/s$:

- Closed section, small end plates $(255mm/1.5c)$,
- Closed section, large end plates $(340mm/2.0c)$,
- Open section, large end plates.

The end plates with different sizes are shown in Fig. 11. Each of the setups was tested for 3 runs from -13° to 14°. Prior to the test the balance was calibrated in lift, drag and pitch axis using weights. The sensor readings were reset to zero at 0° angle of attack before every run. The angle of attack was calibrated using an inclinometer mounted horizontally on the model. A no-wind gravity polar was recorded for both the small and large end plates, and was subtracted from force and moment measurements. The results are compared with aerodynamic polar calculated from XFOIL. Ultimately it was found that the closest result in agreement with XFOIL calculations from the preliminary runs were obtained using the closed section, small end plates setup. The subsequent tests were performed with this setup.

(a) Closed section with $1.5c$ diameter end plates (b) Closed section with $2.0c$ diameter end plates

Figure 11 – Clean model setup at ISAE low-speed wind tunnels

6.3 Clean Configuration

Presented below are the results averaged from test runs of the DAE31 models in clean configurations. Lift coefficient computed from XFOIL and StarCCM+ at the same Reynolds number are superposed. The results are in agreement in the linear lift curve, although slight 3D effect can be observed that produces a lower lift line slope for the experimental curve. The maximal lift coefficient $C_{L_{m0}} = 1.48$ is obtained at 16.5.

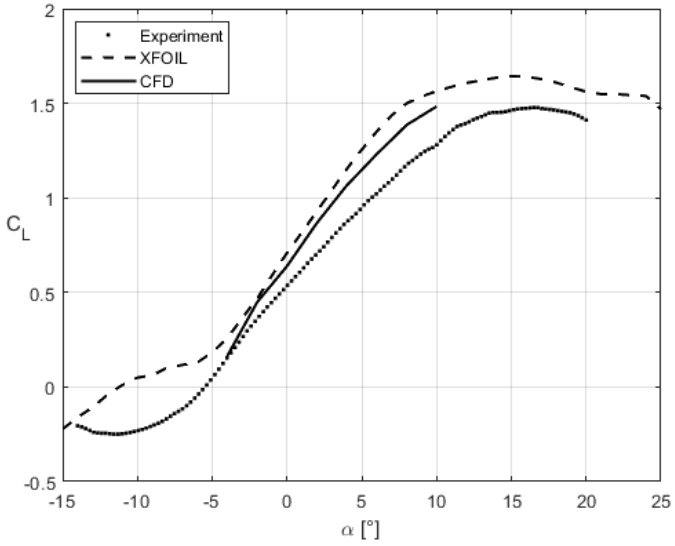

Figure 12 – Clean model results at $Re = 230,000$

6.4 Single-Slotted Flap Model

The single-slotted flap model was tested at the same conditions as the clean model at Reynolds number 2.3×10^5. The results are presented in Fig. 13a and Fig. 13b.

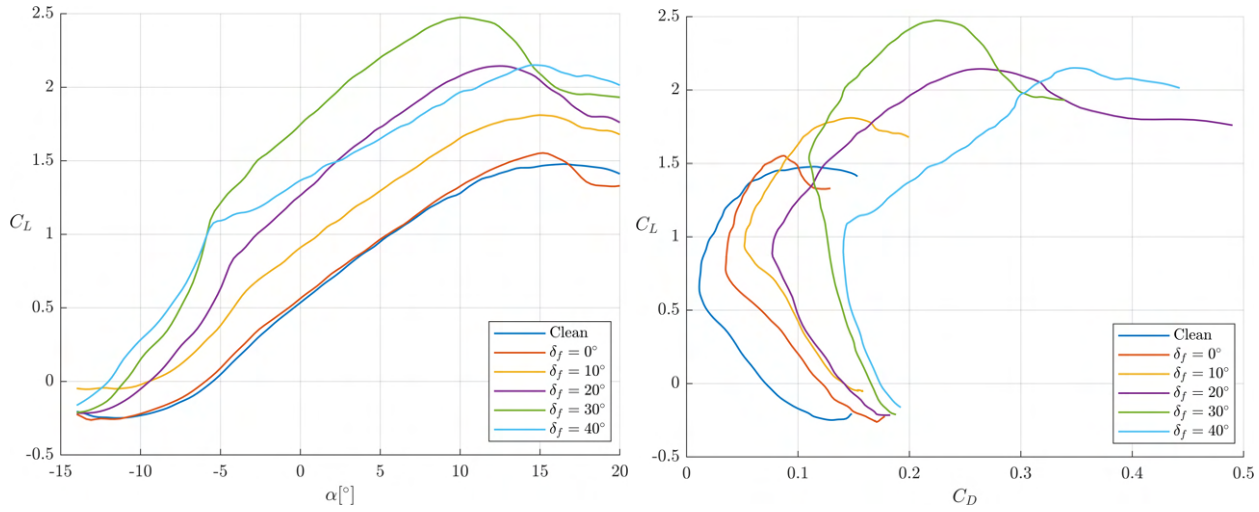

(a) Lift coefficient curve

(b) Aerodynamic polar

Figure 13 – Single-slotted flap aerodynamic characteristics for various flap settings

According to measured lift coefficient curve, lift augmentation is significant for flap deflection up to 30°. Maximal lift coefficient $C_{L_{mf}} = 2.5$ is obtained at $\alpha = 10^\circ$ and $\delta_f = 30^\circ$. At $\delta_f = 40^\circ$, the deployment of the single-slotted flap has reduced lift enhancement and the lift augmentation is comparable to 20° flap deflection.
The aerodynamic polar demonstrates an increase in drag coefficient even when the flap is retracted. There however isn't such significant difference in lift measurement except for the stall region where the single-slotted flap model reached a higher maximal lift coefficient. The drag increase is most probably caused by the form of flap nave, and thus reduces lift to drag ratio.
With increasing flap deflection, the drag polar continues to shift to the right and the minimal drag point moves slightly upwards. At 40° flap deflection, the drag coefficient could double that at $\delta_f = 30^\circ$ for the same lift coefficient. This suggests that although deflecting flap beyond 30° doesn't further enhance lift production, it is effective to increase aerodynamic drag in order to achieve steeper approach angle without significant increase in airspeed.

6.5 Double-Slotted Flap Model

The double-slotted flap model was tested at the same conditions at Reynolds number 2.3×10^5. Different flap settings were tested from the single-slotted flap, and the hinge was adjusted to three different positions $\bar{z}_h$ situated at 5%, 10% and 15% chord length below the mean chord line. The effect of different flap settings for $\bar{z}_h = 15\%$ is first presented in Fig. 14a and Fig. 14b, and the results for other hinge positions are included in the appendix.

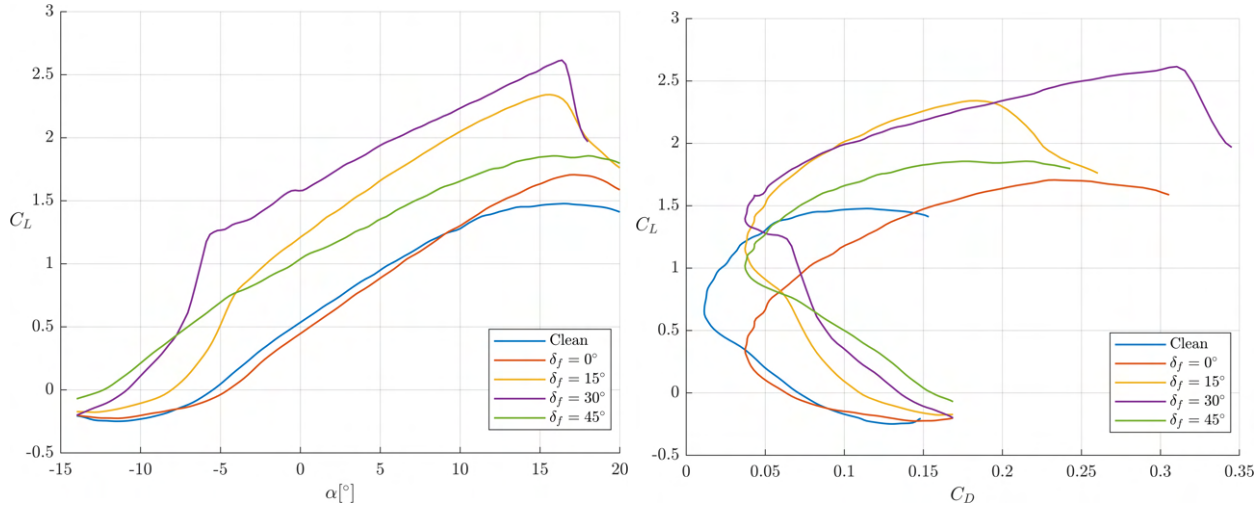

(a) Lift coefficient curve (b) Aerodynamic polar

Figure 14 – Double-slotted flap aerodynamic characteristics for various flap settings, $\bar{z}_h = 15\%$

When retracted, the double-slotted flap model has similar lifting behaviour in linear region, though the discrepancy is larger than that from the single-slotted flap shown in Fig. 13a. The stall region is apparently delayed and maximal lift coefficient could achieve 1.75 without flap deflection.
When deployed, the lift enhancement effect is more complicated than that for single-slotted flap. 15° flap deflection could generate considerable extra lift over the airfoil and maximal lift coefficient is increased to 2.4. The reduction of lift coefficient beyond stall is more rapid than that observed on single-slotted flap. At 30° deflection, the lift enhancement over 15° flap deflection is smaller but the $C_{L_{mf}}$ is still increased to 2.6 at $\alpha = 16^\circ$, after which there is a steep reduction in lift coefficient. At 45° deflection, the difference in lift coefficient from flap retracted configuration reduces with angle of attack, the airfoil observes a benign stall at $C_{L_{mf}} = 1.8$.
The effect of $\bar{z}_h$ at $\delta_f = 30^\circ$ is demonstrated in Fig. 15a and Fig. 15b, and results at other flap settings will be included in the appendix.

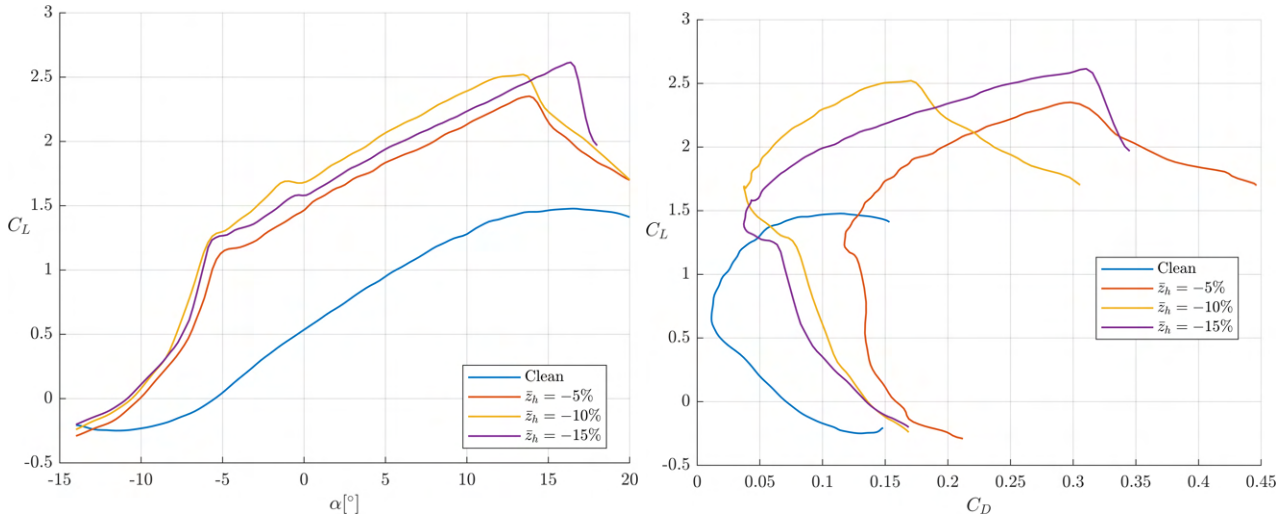

(a) Lift coefficient curve (b) Aerodynamic polar

Figure 15 – Double-slotted flap aerodynamic characteristics for various hinge positions, $\delta_f = 30^\circ$

At 30° flap deflection, significant effect can be observed on the aerodynamics characteristics from different gap sizes. In the linear region, the lift is enhanced by increasing the gap size which is done by lowering hinge point from 5% to 10% chord length. The improvement of flow condition is also evidenced from the decrease of drag coefficient observed in the aerodynamic polar from Fig. 15b. Further lowering the hinge point to 15% chord length doesn't bring increase in lift coefficient in linear

region, however aerodynamic stall is further delayed by 3° compared to when the hinge point was located at 10% chord length. The maximal lift coefficient is thus achieved at 2.6.

6.6 Comparison between Single- and Double-Slotted Flap

Figure. 16a and Fig. 16b present the comparison of single- and double-slotted flap at 0° and 30° flap deflections.

When retracted, the minimal drag coefficient is comparable for both configurations and is higher than the clean DAE31 model. The double-slotted flap achieves its minimal value at lower lift coefficient. The lift to drag ratio is thus lower for double-slotted flap.

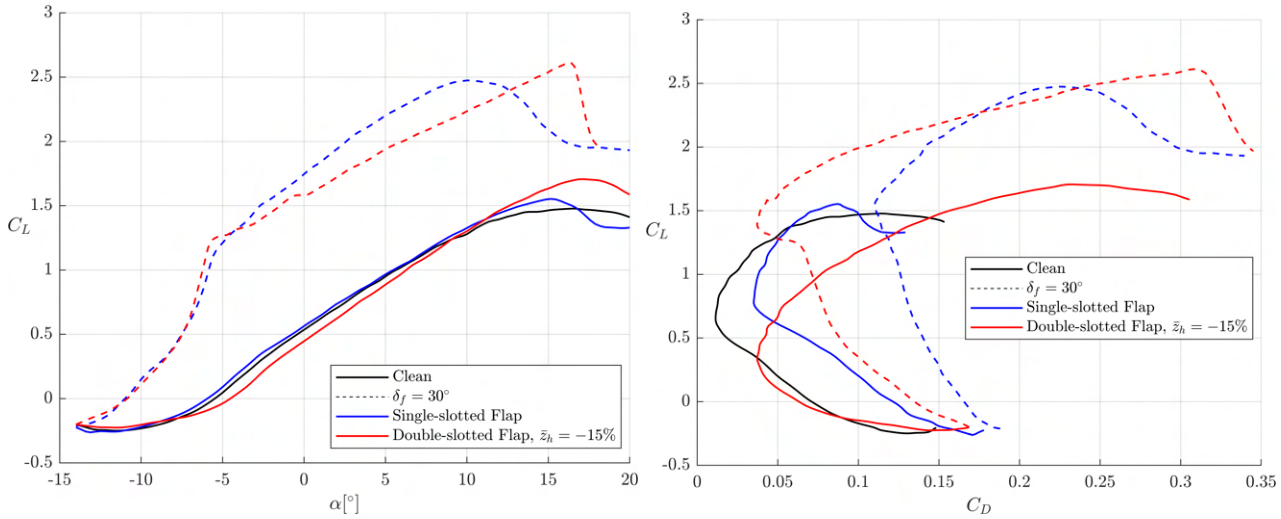

(a) Lift coefficient curve

(b) Aerodynamic polar

Figure 16 – Aerodynamic characteristics for single- and double-slotted flap

At 30° flap deflection, where the best lift enhancement is achieved for both configurations, the lift slope is steeper for single-slotted flap but the delay in stall onset enables the double-slotted flap to reach highest lift coefficient of 2.6. Double-slotted flap also generates up to 70% less drag in linear region, though the drag production is comparable at higher lift coefficient.

The two configurations differ vastly in their stall behaviors. The single-slotted flap reaches stall onset at 10° followed by a relatively gentle reduction in lift coefficient. The double-slotted flap retains good linearity of lift coefficient curve up until 16° where a shart reduction occurs.

These behaviours can also be confirmed from the photo captured during experiment upon stall onset. Tufts were attached to both models in order to visualise the flow field near airfoil surface. In Fig. 17a, flow separation on the single-slotted flap configuration initiated at the trailing edge of main element, however the separated region has yet dominated the airfoil surface, thus yielding more benign behaviour. The tufts visualisation for double-slotted flap is shown in Fig. 17b. The flow is separated well upstream that almost all tufts on the main element were disturbed, causing the sharp reduction in lift. The flow around the flap section however remained attached.

(a) Single-slotted flap (b) Double-slotted flap

Figure 17 – Flow visualisation upon stall onset

7. Numerical Analysis

A numerical study is conducted using STARCCM+ on single- and double-slotted flap configurations. The objective of the numerical study is to obtain high resolution flow field data free from windtunnel blockage and wall effects. Despite the use of end plates, 3D effects from wind tunnel walls cannot be entirely eliminated, and thus high resolution numerical studies are beneficial to make detailed study of the refined configuration.

7.1 Domain and Solver Settings

A conventional circular arc domain is used for the simulation with an arc radius of $5c$ and $10c$ in the downstream direction. The arc is defined as the velocity inlet and the downstream boundary is defined as a pressure outlet. An implicit unsteady solver is used to capture the unsteady flow downstream of the flap. K-ω SST model is used as the turbulence model to include laminar-turbulence transition. The computation domain was discretised using quadrilateral mesh as presented in Fig. 18. A wake refinement region spreads downstream for $5c$ with a spread angle of $5°$.

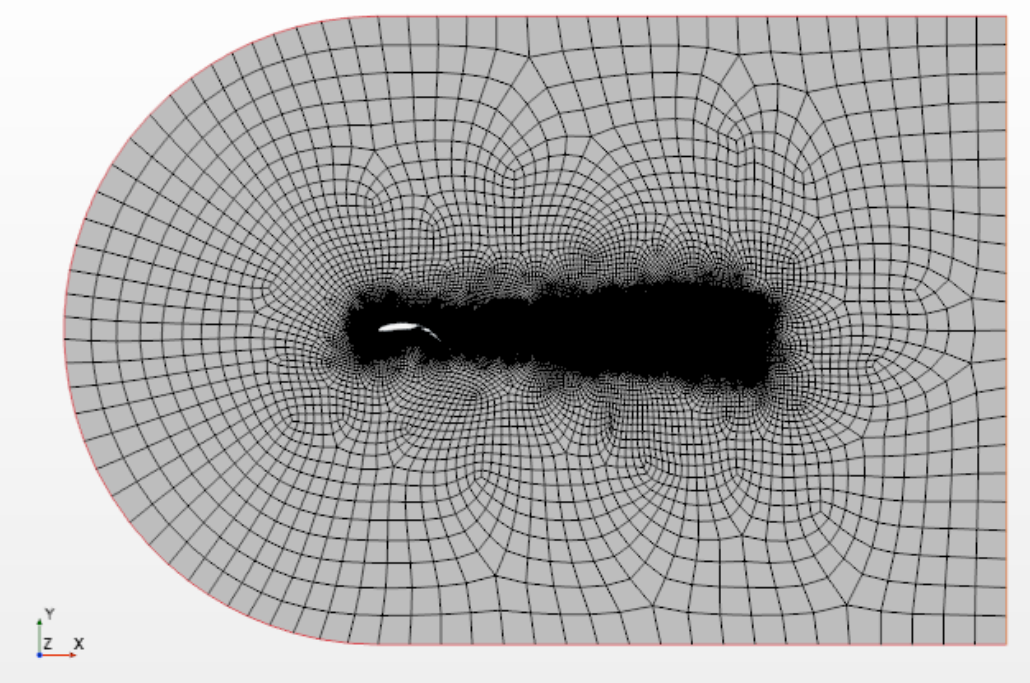

Figure 18 – Computational domain mesh

Close-up Figure. 19 demonstrates the gradual transition of near wall prism layer to far field region. The prism layer was set-up so that wall $y+ \sim 1$ where possible, and all-$y+$ treatment option was used to provide best solution of boundary layer.

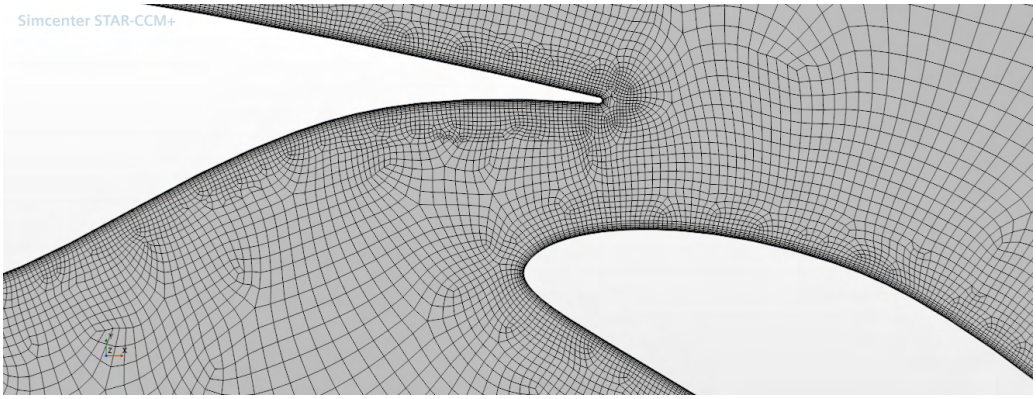

Figure 19 – Computational domain: airfoil closeup mesh

In addition, a 3D simulation was performed to inform comparison between experimental data and numerical results. The simulation retains the windtunnel and $1.5c$ diameter end plate dimensions to include wall effects, the test section extends 3 chord length unpstream and 5 chord length downstream. Single-slotted flap was modelled with 10° angle of attack and 30° flap deflection. The half-model domain contains 2.5 million cells and the associated boundary conditions are illustrated in Fig. 20.

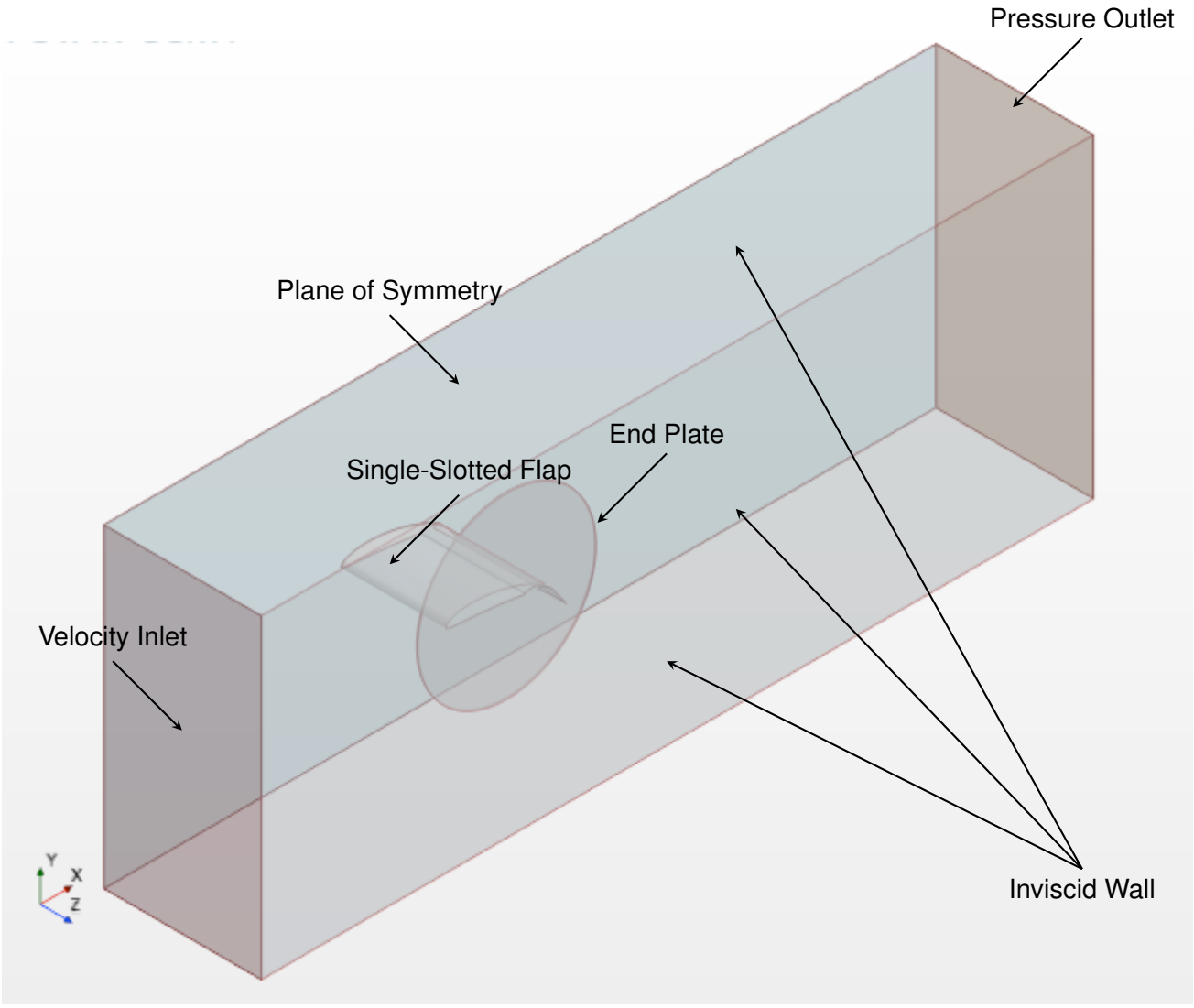

Figure 20 – Computational domain for 3D simulation

7.2 Mesh Convergence

A mesh convergence study was performed for clean DAE31 airfoil with three mesh density levels. The coarse mesh has 32600 cells ; the medium mesh has 46000 cells and the fine mesh consists 70586 cells. The results shown in Fig. 21] at $\alpha = 2^\circ$ suggests asymptotic trends in drag coefficient prediction and the relative difference falls below 5% convergence bound. Therefore the mesh was considered valid for the current study, and the medium density mesh was used in subsequent analyses.

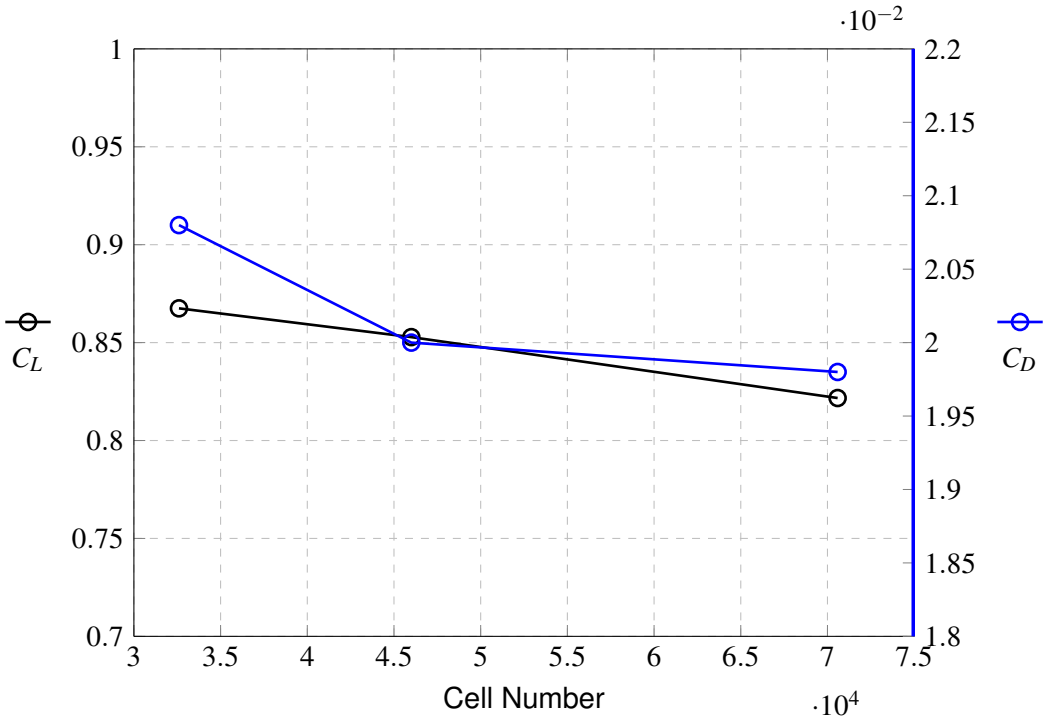

Figure 21 – Lift and drag coefficient of DAE31 airfoil computed with different mesh density

7.3 Results and Discussion

7.3.1 Maximal lift coefficient

The single- and double-slotted flap configurations were computed at $\alpha = 10^\circ$, $Re = 3 \times 10^5$ and $\delta_f = 30^\circ$, which are the most capable to generate lift according to experimental data. The lift coefficient of both configurations are denoted as circle symbol together with experimental measurements in Fig. 22.

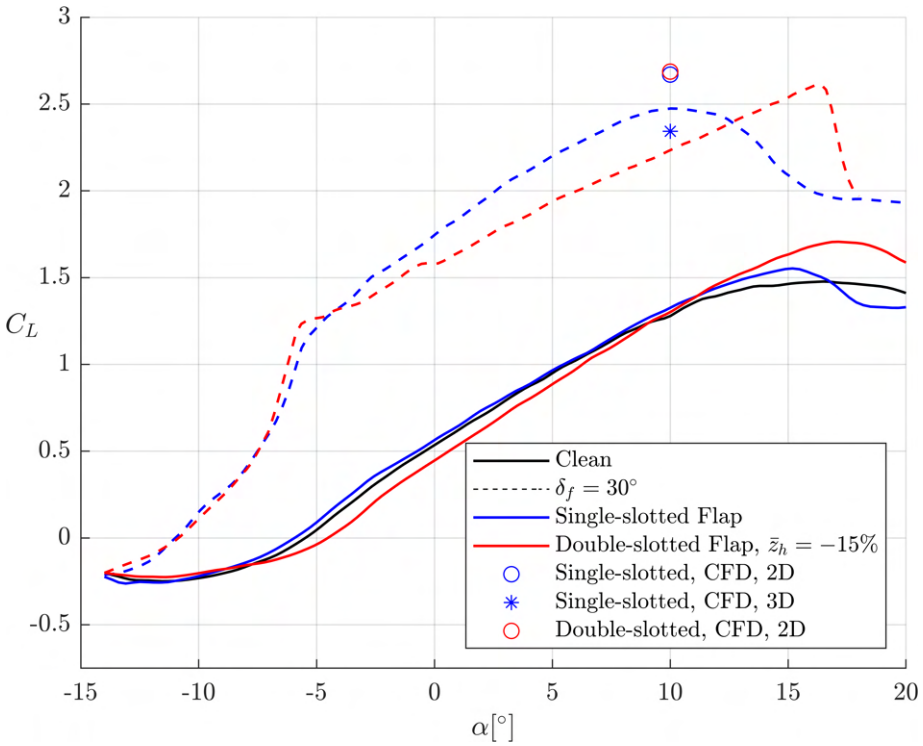

Figure 22 – Calculated lift coefficient of single- and double-slotted flap configurations

The lift coefficients from numerical studies were notably larger than the experimental data. In comparison, the lift coefficient from 3D simulation at the same condition is found to be 2.343, which lies closer to the experimental results. This indicates that 3D effects aren't completely eliminated by the use of end plates.

7.3.2 Three dimensional effects

The ratio $\tau = \frac{C_{L_{3D}}}{C_{L_{2D}}}$ is a measure of 3D effects between untwisted finite straight wing of identical airfoil [18], the ratio is found to be $\tau_{ss} = 0.926$ for single-slotted flap and $\tau_{ds} = 0.834$ for double-slotted flap. To further study the 3D flow condition over the airfoil model, pressure data was extracted from main and flap element surface in order to calculate spanwise lift distribution and local circulation, as presented in Fig. 23.

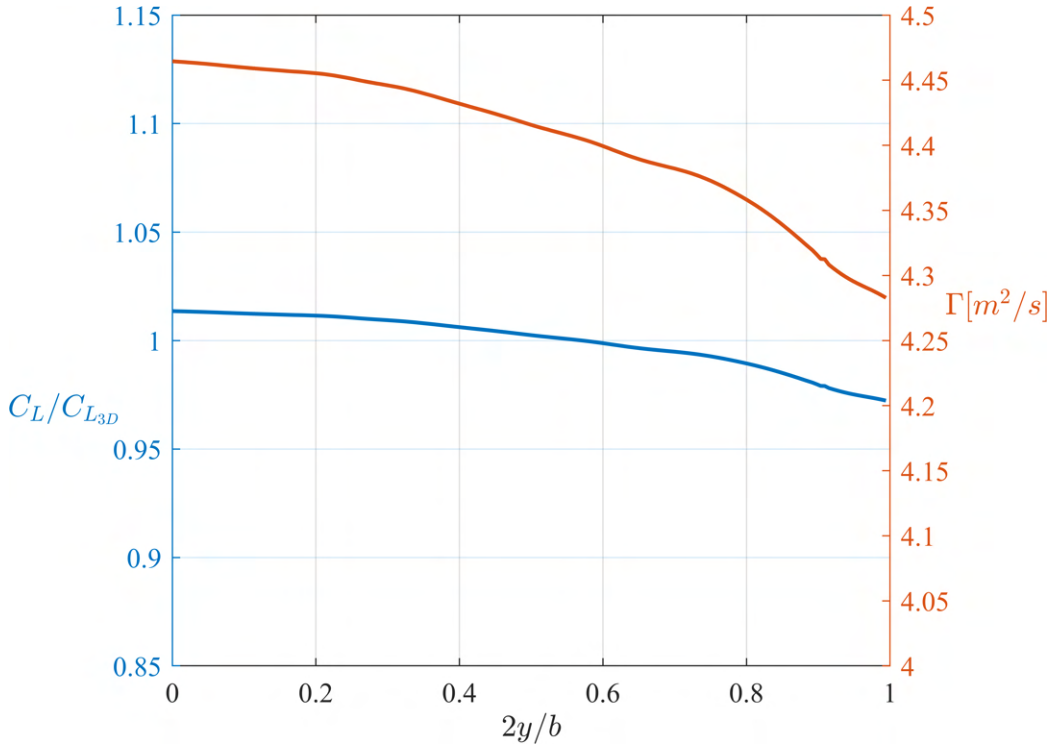

Figure 23 – Spanwise lift and circulation distribution of 3D single-slotted flap simulation

Local lift coefficient in Fig. 23 stays close to total lift coefficient $C_{L_{3D}}$ over majority of span stations, however the value reduces noticeably towards the wing tip. The circulation distribution allows for equivalent aspect ratio λ^*. Fitting the circulation distribution to Fourier sine series :

$$\Gamma(\theta) = 2bV_\infty \left(A_0 + \sum_{n=1}^{N} A_n \sin n\theta \right) \tag{6}$$

where variable transformation $y = -\frac{b}{2}\cos\theta$. $A_0 \neq 0$ because the presence of end plate. The Oswald coefficient can then be calculated from the higher-order Fourier coefficients.

$$e = \frac{1}{1+\delta} = \frac{1}{1+\sum_{n=2}^{N} n\left(\frac{A_n}{A_1}\right)^2} \tag{7}$$

For the 3D simulation, Oswald coefficient is estimated to be 0.905. For non-twisted straight wing segment with identical airfoil, the ratio τ is the quotient of 2D lift gradient over 3D lift gradient, and is proved to be related to wing aspect ratio :

$$\tau = \frac{1}{1+\frac{2}{\lambda^* e}} \tag{8}$$

From 2D and 3D numerical results for single-slotted flap $\tau_{CFD} = 0.877$, and the equivalent aspect ratio of the model with end plates can then be solved to be $\lambda^* = 15.9$, which is much higher than the actual model aspect ratio $\lambda = 1.76$.

The higher τ calculated between experimental and numerical results demonstrates that the end plates compensate partly the finite span effects. The 3D effects can still accounts for $8-20\%$ error for high-lift conditions. Interestingly, the 3D effect appears to be stronger for double-slotted flap configurations. This is probably caused by wall boundary layer interaction between end plate and flap gap, which affects double-slotted flap configuration more.

Iso-surface of Q-criterion around the single-slotted flap in 3D simulation is shown in Figure. 24. Q-criterion is a parameter for vortex identification, and thus it demonstrates the vortical structure around the gap between main and flap element. The region of vortical layer at the flap leading edge remains small and constant in stream-wise expansion close to the centre span. This region however expands

rapidly in downstream direction closer to end plate, and eventually joins the vortex system formed at the junction between upper surface and end plate. This implies increased boundary layer thickness at the flap leading edge which may adversely affect the flow condition at the gap as shown in section. 4.

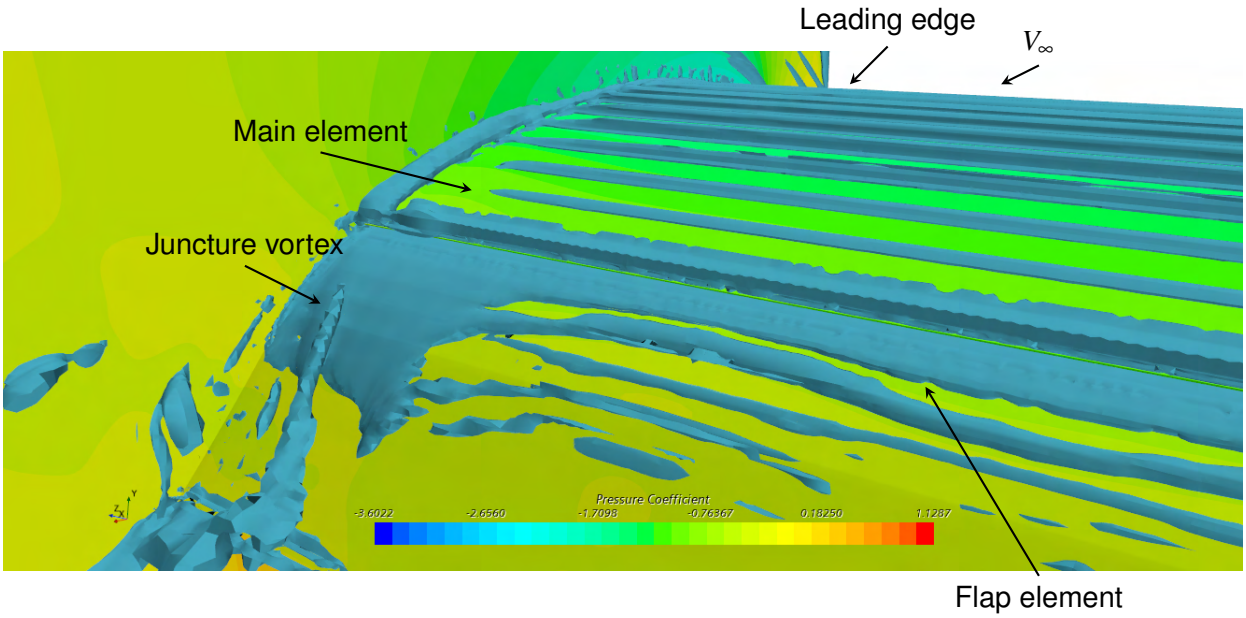

Figure 24 – Pressure coefficient and Q-criterion iso-surface

8. Conclusions

This research draws several conclusions of the aerodynamic phenomena and design methodology of high-lift devices design for low Reynolds number applications :

- Lift generation is expected to be reduced due to boundary layer carrying capability and simplification of mechanism kinematics.
- Semi-empirical methods are less reliable for low Reynolds number designs due to database availabilities, and current methods tend to yield wide range of results.
- Potential methods or Euler-based solver such as MSES remain an efficient tool for detailed design of airfoil profile and kinematics. However the results are less reliable and/or more restricted due to separation treatment.
- At low Reynolds number, the gap size and overlap length are strongly coupled to maximise lift generation, the sensitivity of design parameters are usually within 1% of total chord length. The highest lift coefficient design usually has a small overlap.
- Experimental methods provide essential validation for high-lift devices design, and low-speed windtunnels are sufficient to simulate operating conditions. However the results tend to underestimate lift generation due to 3D effects, and the effects are stronger particular for more complex configurations such as double-slotted flaps.

9. Copyright Statement

A Double-Slotted Flap Experimental Results for Various Hinge Position

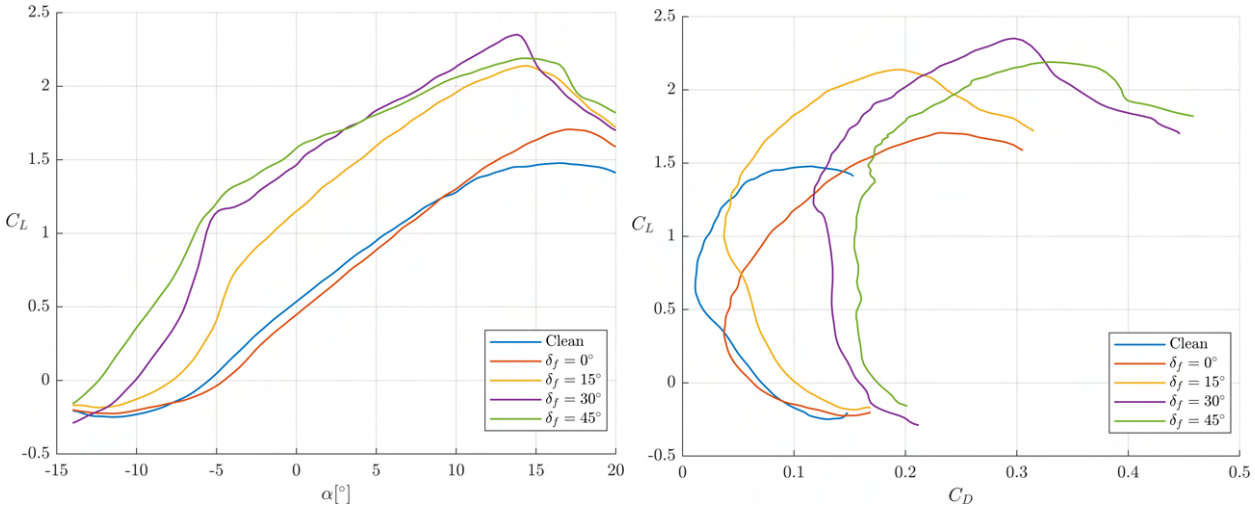

(a) Lift coefficient curve (b) Aerodynamic polar

Figure 25 – Double-slotted flap aerodynamic characteristics for $\bar{z}_h = -5\%$

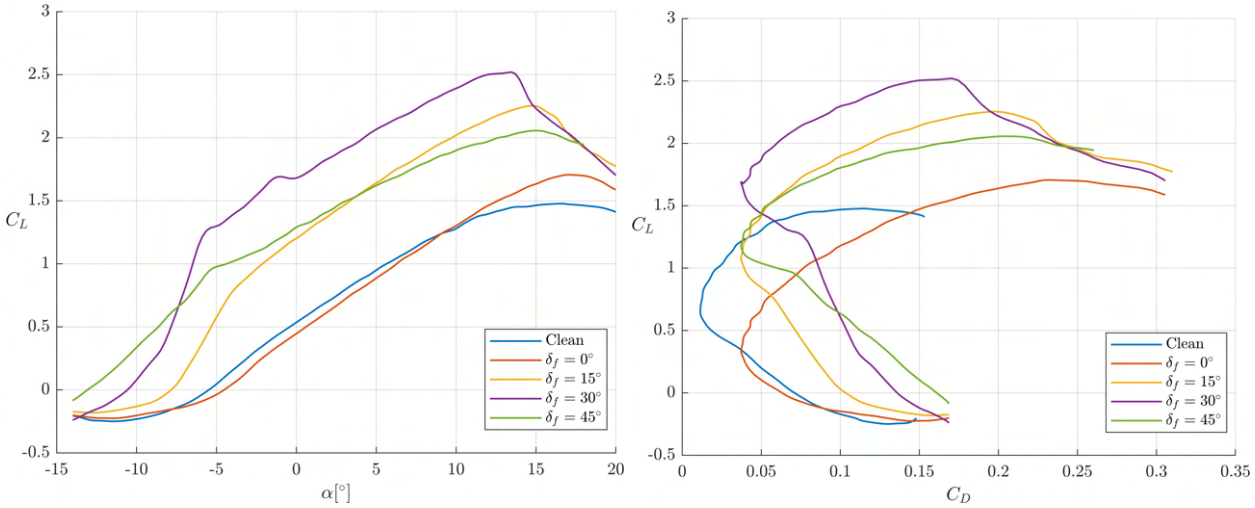

(a) Lift coefficient curve (b) Aerodynamic polar

Figure 26 – Double-slotted flap aerodynamic characteristics for $\bar{z}_h = -5\%$

B Double-Slotted Flap Experimental Results for Various Flap Settings

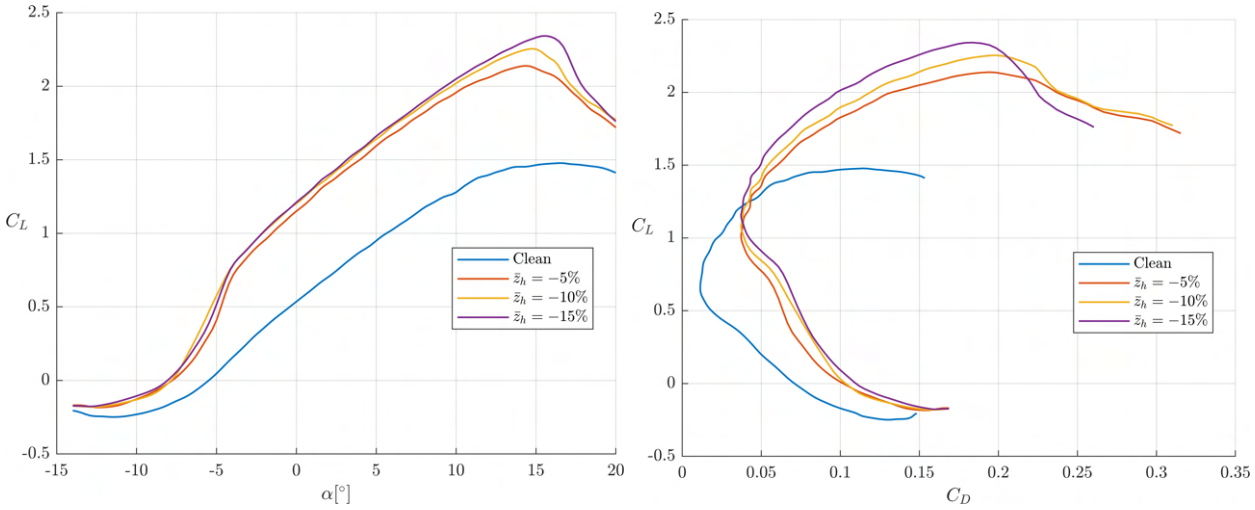

(a) Lift coefficient curve (b) Aerodynamic polar

Figure 27 – Double-slotted flap aerodynamic characteristics for $\delta_f = 15°$

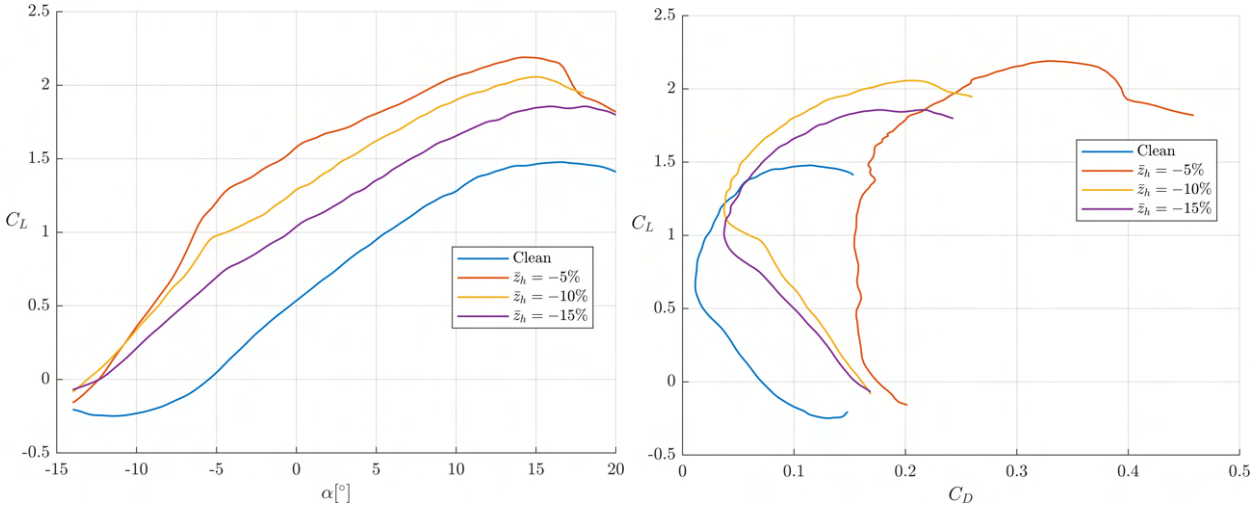

(a) Lift coefficient curve (b) Aerodynamic polar

Figure 28 – Double-slotted flap aerodynamic characteristics for $\delta_f = 45°$

Acknowledgments

The authors would like to thank Delair for the financial support of the project as well Prof. Jean-Marc Moschetta and Mr. Marc Grellet for facilitating the use of the wind tunnels and their valued input throughout the project. The authors would also like to thank Dr. Murat Bronz for providing access to the Windshape facility which was the start of the experimental test and highlighted important issues with the fabrication of the wing models and test setup. The design study was carried out by MSES software under licence ID 4916600, and the authors would like to thank MIT Technology Licensing Office and Prof. Mark Drela for their assistance. Lastly Mr. Karim Fayez would like to thank Mr. Emilien Delagarde for his contribution on the fabrication of the models used in the experiments.

References

[1] Finck, R., "USAF (United States Air Force) Stability and Control DATCOM (Data Compendium)," Tech. rep., MCDONNELL AIRCRAFT CO ST LOUIS MO, 1978.

[2] Smith, A. M., "High-lift aerodynamics," *Journal of Aircraft*, Vol. 12, No. 6, 1975, pp. 501–530.

[3] Hayter, N.-L. F. and Kelly, J. A., "Lift and Pitching Moment at Low Speeds of the Naca 64A010 Airfoil Section Equipped with Various Combinations of a Leading-edge Slat, Leading-edge Flap, Split Flap, and Double-slotted Flap," Tech. Rep. NACA-TN-3007, NACA, 1953.

[4] Peter, K., "High-Lift systems on commercial subsonic airliners," Tech. Rep. NASA CR-4746, NASA, 1996.

[5] Cahill, J. F., "Summary of section data on trailing-edge high-lift devices," Tech. Rep. NACA-TR-938, NACA, 1949.

[6] Young, A., "The Aerodynamic Characteristics of Flaps." Tech. Rep. No. 2622, British ARC, 1947.

[7] Gudmundsson, S., *General aviation aircraft design: Applied Methods and Procedures*, Butterworth-Heinemann, 2013.

[8] Yamada, Y., Vasilieva, I., Takayama, A., Fukushima, E. F., and Endo, G., "Circulation-controlled high-lift wing for small unmanned aerial vehicle," *ROBOMECH Journal*, Vol. 2, No. 1, 2015, pp. 1–11.

[9] Selig, M. S. and Guglielmo, J. J., "High-lift low Reynolds number airfoil design," *Journal of aircraft*, Vol. 34, No. 1, 1997, pp. 72–79.

[10] Jones, A., Bakhtian, N., and Babinsky, H., "Low Reynolds number aerodynamics of leading-edge flaps," *Journal of Aircraft*, Vol. 45, No. 1, 2008, p. 342.

[11] Oliveira, A. D. S., *Low Reynolds Number Fowler Flap Design*, Ph.D. thesis, Universidade da Beira Interior (Portugal), 2017.

[12] Garner, H., Bean, G., Birch, N., Dexter, P., Dovey, J., Garry, K., Graham, D., Green, M., Horton, H., Hurst, D., Jones, P., Karling, K., Maurel, M., Newbold, C., Newton, J., Sanderson, R., Sewell, A., Smith, M., and Tweedie, J., "Introduction to the estimation of the lift coefficients at zero angle of attack and at maximum lift for aerofoils with high-lift devices at low speeds," Tech. Rep. 94026, Engineering Sciences Data Unit, 1994.

[13] Garner, H., Bean, G., Birch, N., Dexter, P., Dovey, J., Garry, K., Graham, D., Green, M., Horton, H., Hurst, D., Jones, P., Karling, K., Maurel, M., Newbold, C., Newton, J., Sanderson, R., Sewell, A., Smith, M., and Tweedie, J., "Increments in aerofoil lift coefficient at zero angle of attack and in maximum lift coefficient due to deployment of a double-slotted or triple-slotted trailing-edge flap, with or without a leading-edge high-lift device, at low speeds," Tech. Rep. 94031, Engineering Sciences Data Unit, 1994.

[14] Daniel, P. R. et al., *Aircraft design: a conceptual approach*, American Institute of Aeronautics and Astronautics Inc, 1992.

[15] Drela, M., *A User's Guide to MSES 3.05*, MIT Press, 2007. `https://web.mit.edu/drela/Public/web/mses/mses.pdf`.

[16] Garner, H., Bean, G., Birch, N., Dexter, P., Dovey, J., Garry, K., Graham, D., Green, M., Horton, H., Hurst, D., Jones, P., Karling, K., Maurel, M., Newbold, C., Newton, J., Sanderson, R., Sewell, A., Smith, M., and Tweedie, J., "Increments in aerofoil lift coefficient at zero angle of attack and in maximum lift coefficient due to deployment of a single-slotted trailing-edge flap, with or without a leading-edge high-lift device, at low speeds," Tech. Rep. 94030, Engineering Sciences Data Unit, 1994.

[17] "MIT Human Powered Aircraft and Hydrofoil info web page," , 2007. `https://web.mit.edu/drela/Public/web/hpa/`.

[18] Anderson, J. and Hughes, W., *Fundamentals of Aerodynamics*, McGraw-Hill Education, 2009.